$BaFe_{12}O_{19}$ Single-Particle-Chain Nanofibers: Preparation, Characterization, Formation Principle, and Magnetization Reversal Mechanism

Junli Zhang,[†] Jiecai Fu,[†] Fashen Li,[†] Erqing Xie,[†] Desheng Xue,[†] Nigel J. Mellors,[‡] and Yong Peng[†,‡,*]

[†]Key Laboratory of Magnetism and Magnetic Materials of Ministry of Education, Lanzhou University, Lanzhou 730000, People's Republic of China, and [‡]Nano Materials Group, School of Computing, Science and Engineering, University of Salford, Greater Manchester M5 4WT, United Kingdom

ABSTRACT $BaFe_{12}O_{19}$ single-particle-chain nanofibers have been successfully prepared by an electrospinning method and calcination process, and their morphology, chemistry, and crystal structure have been characterized at the nanoscale. It is found that individual $BaFe_{12}O_{19}$ nanofibers consist of single nanoparticles which are found to stack along the nanofiber axis. The chemical analysis shows that the atomic ratio of Ba/Fe is 1:12, suggesting a $BaFe_{12}O_{19}$ composition. The crystal structure of the $BaFe_{12}O_{19}$ single-particle-chain nanofibers is proved to be M-type hexagonal. The single crystallites on each $BaFe_{12}O_{19}$ single-particle-chain nanofibers have random orientations. A formation mechanism is proposed based on thermogravimetry/differential thermal analysis (TG-DTA), X-ray diffraction (XRD), and transmission electron microscopy (TEM) at six temperatures, 250, 400, 500, 600, 650, and 800 °C. The magnetic measurement of the $BaFe_{12}O_{19}$ single-particle-chain nanofibers reveals that the coercivity reaches a maximum of 5943 Oe and the saturated magnetization is 71.5 emu/g at room temperature. Theoretical analysis at the micromagnetism level is adapted to describe the magnetic behavior of the $BaFe_{12}O_{19}$ single-particle-chain nanofibers.

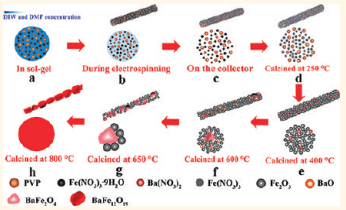

KEYWORDS: $BaFe_{12}O_{19}$ · electrospinning · single-particle-chain nanofibers · formation principle · CBED · EDX elemental mapping · high saturation magnetization · magnetic reversal mechanism

Nanoscale magnetic ferrite materials have attracted much attention in recent years due to their unique magnetic and electrical properties and chemical stabilities.[1,2] These properties are significant not only from a fundamental point of view, for example, blocking behavior, nanoscale confinement, and nanomagnetism,[3−5] but also for their potential applications, such as high-density data storage, spin-electronics, bioseparation, magnetic resonance imaging, and magnetically guided drug delivery systems.[6−10] Barium ferrite ($BaFe_{12}O_{19}$) is one member of the ferrite family with significant material qualities such as high Curie temperature, large magnetization, large magnetocrystalline anisotropy, high coercivity, and excellent chemical stability.[11] It has been widely adopted as a traditional permanent magnet and also recently used as high-density magnetic and magneto-optical recording media and microwave filters.[12−15] Since the magnetic properties of $BaFe_{12}O_{19}$ strongly depend on their particle size, shape, and homogeneity, various methods, including microwave-induced, laser deposition, microemulsion, and nanopatterning technique,[16−19] have been used to prepare nanoscale $BaFe_{12}O_{19}$ to improve their magnetic properties. These manufacturing techniques have tended to focus on nanoscale particles. There are few reports on one-dimensional (1D) $BaFe_{12}O_{19}$ nanowires which were mainly fabricated by a template method using nanoporous anodic aluminum oxide films as the template. However, the diffusion of aluminum ions in $BaFe_{12}O_{19}$ nanowires often causes heterogeneous impurities, and nanowires often display a low aspect ratio. It is also difficult to realize a practical industrial production and currently lack sophisticated nanotechnologies to develop these free-standing nanowire building blocks into functional nanodevices. The ever-increasing applications of magnetic nanowires in the new field of biomagnetics and high-density data storage media demand novel fabrication methods which have a promising potential to realize large-scale production of high-quality free-standing 1D magnetic nanowires. Electrospinning is believed to provide this possibility.

* Address correspondence to pengy@lzu.edu.cn.

Received for review November 8, 2011 and accepted February 3, 2012.

Published online February 03, 2012
10.1021/nn204342m

© 2012 American Chemical Society

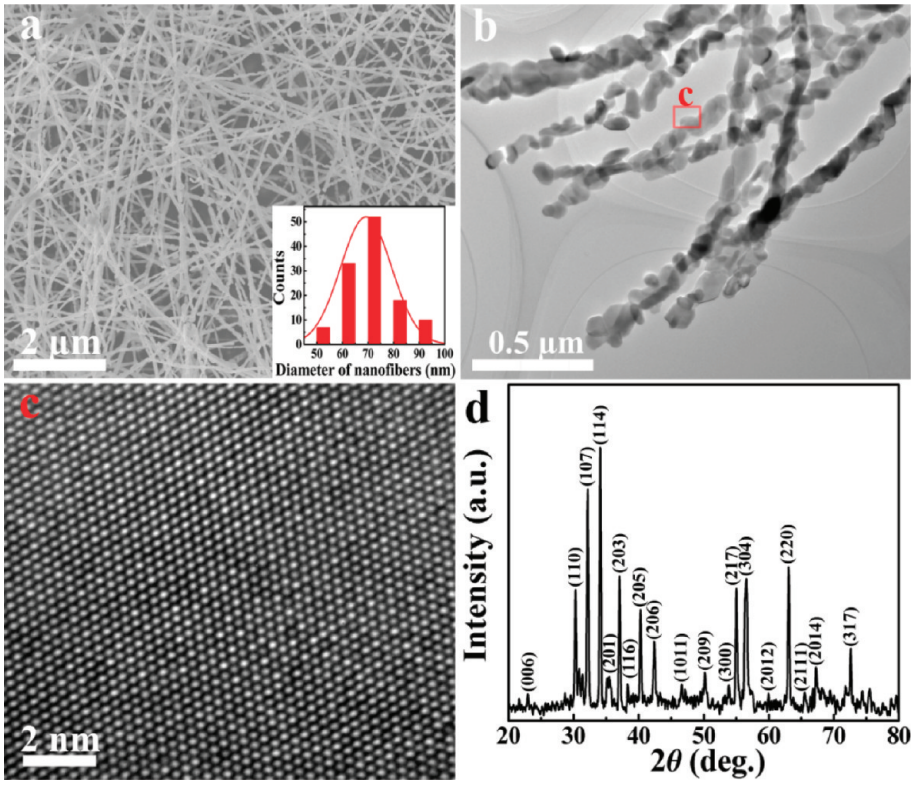

Figure 1. (a) Representative SEM image of $BaFe_{12}O_{19}$ nanofibers. Inset shows a quantitative analysis of their diameter distribution. (b) Bright-field TEM image of individual $BaFe_{12}O_{19}$ single-particle-chain nanofibers calcined in air at 800 °C for 2 h. (c) Lattice-resolution HRTEM image of the particle marked by a red square in (b). (d) XRD pattern detected from a large amount of the $BaFe_{12}O_{19}$ nanofibers calcined at 800 °C for 2 h.

Electrospinning is a process by which very fine fibers (with diameter on the micro- or nanoscale and lengths up to kilometers) are drawn from a liquid by an electrical charge. The first significant report of electrospinning to produce fibers dates from 1934 when a patent filed by A. Formhals was issued which described electrospinning as a process for forming fine textile fibers.[20] Electrospinning combined with heating treatments has been widely adopted to prepare various 1D nanomaterials because of the simple manufacturing method, low cost, and relatively high production rate. The applicability of many types of materials include metals, metal oxides, and ferrite nanofibers.[21−25] However, there are rarely reports on M-type $BaFe_{12}O_{19}$ nanofibers. It is believed to be because forming 1D M-type $BaFe_{12}O_{19}$ nanofibers involves a very high temperature heating treatment under zero local spatial confinement, which is extremely not conducive to forming a 1D structure whether at the microscale or nanoscale.

In this work, we present a fabrication method of $BaFe_{12}O_{19}$ single-particle-chain nanofibers prepared using a combined technique of electrospinning and high-temperature heating treatment for the first time. The morphology, structure, chemical and magnetic characterization, and growth mechanism of the $BaFe_{12}O_{19}$ single-particle-chain nanofibers have been systemically investigated. It is believed that the new structural form of the single-particle-chain nanofibers is significant and will contribute to expanding the applications of $BaFe_{12}O_{19}$ into the new field of biomagnetics and high-density data storage media.

RESULTS AND DISCUSSION

Morphological and Chemical Analysis of $BaFe_{12}O_{19}$ Single-Particle-Chain Nanofibers. The morphologies of $BaFe_{12}O_{19}$ nanofibers calcined at 800 °C for 2 h were observed by SEM and TEM. Figure 1a shows a representative SEM image of the calcined $BaFe_{12}O_{19}$ nanofibers. Continuous structure and virtually uniform diameter can be seen in each nanofiber after the PVP was removed by the calcination process. The average length for the majority of the nanofibers is approximately 150 μm, while the average diameter is for 70 nm. The quantitative analysis (inset of Figure 1a) shows that the diameter of the $BaFe_{12}O_{19}$ nanofibers, measured on average 70 nm, ranges from 50 to 100 nm.

Figure 1b displays a TEM image of several $BaFe_{12}O_{19}$ nanofibers, which provides a further insight into their microstructure. It is clearly seen that individual $BaFe_{12}O_{19}$ nanofibers consist of single nanoparticles stacked along the nanofiber axis. Therefore, the nanofibers are named $BaFe_{12}O_{19}$ single-particle-chain nanofibers in this work. Individual $BaFe_{12}O_{19}$ single-particle-chain nanofibers have a continuous structure and uniform diameter, which is in good agreement

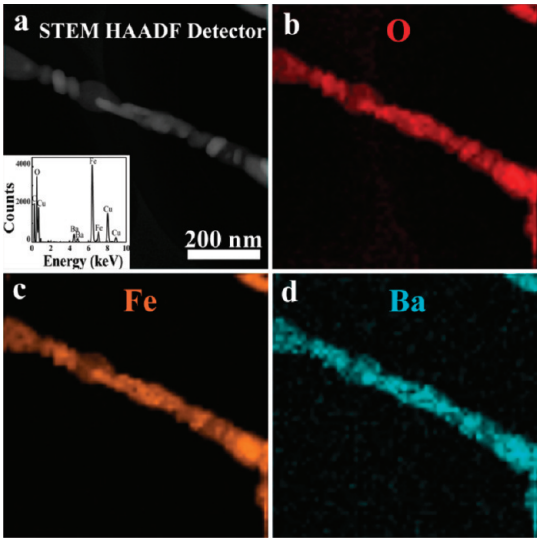

Figure 2. EDX mappings of individual $BaFe_{12}O_{19}$ single-particle-chain nanofiber. (a) Representative STEM-HAADF image of a single $BaFe_{12}O_{19}$ nanofiber. Inset shows the EDX spectrum acquired from the area in Figure 1b. (b) Oxygen mapping. (c) Iron mapping. (d) Barium mapping.

with the above SEM observation. It is known that the critical single-domain radius of $BaFe_{12}O_{19}$ particles is approximately 290 nm,[26] which suggests that each particle on the $BaFe_{12}O_{19}$ single-particle-chain nanofibers is a magnetically single domain.

Figure 1c shows a lattice-resolution HRTEM image of the single nanoparticle marked by red square in Figure 1b, revealing a single-crystalline structure. The interplanar spacing is measured to be 0.263 nm, consistent with the (114) crystallographic orientation of M-type hexagonal $BaFe_{12}O_{19}$. The SAED experiments which are presented later demonstrate that the M-type hexagonal structure is preserved in the $BaFe_{12}O_{19}$ single-particle-chain nanofibers. The crystal structure was further investigated by XRD technique. Figure 1d shows a typical XRD spectrum of the $BaFe_{12}O_{19}$ single-particle-chain nanofibers calcined at 800 °C for 2 h. The corresponding XRD diffraction peaks can be indexed to (006), (110), (107), (114), (201), (203), (116), (205), (206), (1011), (209), (300), (217), (304), (2012), (220), (2111), (2014), and (317) planes. This suggests that the hexagonal structure of bulk $BaFe_{12}O_{19}$ is preserved in the $BaFe_{12}O_{19}$ single-particle-chain nanofibers, which is consistent with the crystal characterization using TEM. There is no impurity phases presented in this spectrum, indicating a pure chemical phase of $BaFe_{12}O_{19}$.

The chemistry of the $BaFe_{12}O_{19}$ single-particle-chain nanofibers was characterized using EDX and STEM mapping on a 300 kV HRTEM. The inset of Figure 2a shows a representative EDX spectrum obtained from the corresponding area in Figure 1b. The barium, iron, and oxygen peaks come from the nanofiber specimen. As the EDX technique is not accurate for analyzing the low atomic number (low Z), only the atomic ratio of barium and iron was simulated in this spectrum in order to avoid an error. Quantitative analysis of this spectra indicates a 1:12 atomic ratio of Ba/Fe, inferring a $BaFe_{12}O_{19}$ composition for the nanofibers prepared under our experimental conditions. The copper and carbon come from the holey carbon coated copper grids, which was confirmed by EDX of an empty holey carbon coated copper grid.

The chemical element distributions of $BaFe_{12}O_{19}$ nanofibers were further studied by HAADF-STEM and EDX elemental mapping analysis (Figure 2) techniques. Figure 2a shows a representative HADDF-STEM image of a single $BaFe_{12}O_{19}$ single-particle-chain nanofiber. The contrast of incoherent high-resolution HADDF-STEM images depends directly on the sample atomic number Z and thickness for the materials; in the nanofiber image, a pure chemical phase is revealed, and the individual $BaFe_{12}O_{19}$ nanofiber is composed of single crystals of various sizes stacking along the nanofiber axis. Figure 2b–d displays the corresponding EDX mappings of oxygen (K_α, 0.52 keV), iron (K_α, 6.4 keV), and barium (L_α, 4.47 keV) elements, respectively. It is seen that the elements O, Fe, and Ba are evenly distributed throughout the whole nanofiber, revealing a uniform chemical phase.

Figure 3 shows a detailed structural investigation of the $BaFe_{12}O_{19}$ single-particle-chain nanofibers using TEM and convergent beam electron diffraction (CBED) techniques. The large-magnified TEM image (Figure 3a) reveals that the individual $BaFe_{12}O_{19}$ nanofiber is composed of single nanocrystallites stacking alternatively along the nanofiber axis. The size of these nanocrystallites ranges from 40 to 80 nm confirmed by the TEM observations. CBED using a 0.5 nm spot size configuration is believed to be used for the first time to analyze the crystal structure of single $BaFe_{12}O_{19}$ crystallites on a single nanofiber. The top-left inset shows the CBED pattern of the particle marked by a red circle in Figure 3a, revealing a hexagonal close packing (hcp) structure with ⟨110⟩ orientation. The bottom-right inset shows the CBED pattern of a particle marked by a green circle, revealing a ⟨100⟩ orientation of the hcp structure. The representative lattice-resolution HRTEM image of the interface between the two neighbor particles is shown in Figure 3b, indicating consistent crystal orientations and serial planes also confirmed by CBED analysis. More boundary HRTEM results (see Figure S2 in the Supporting Information for details) prove that the single crystallites of the $BaFe_{12}O_{19}$ single-particle-chain nanofibers have a random orientations, which is not consistent as previously reported.[27]

Formation Principle of the $BaFe_{12}O_{19}$ Single-Particle-Chain Nanofibers. The formation mechanism, including chemical reactions and phase transformations, of the $BaFe_{12}O_{19}$ single-particle-chain nanofibers were analyzed by TG-DTA, XRD, and TEM. Figure 4 illustrates the typical TG-DTA curves from the transformation of the

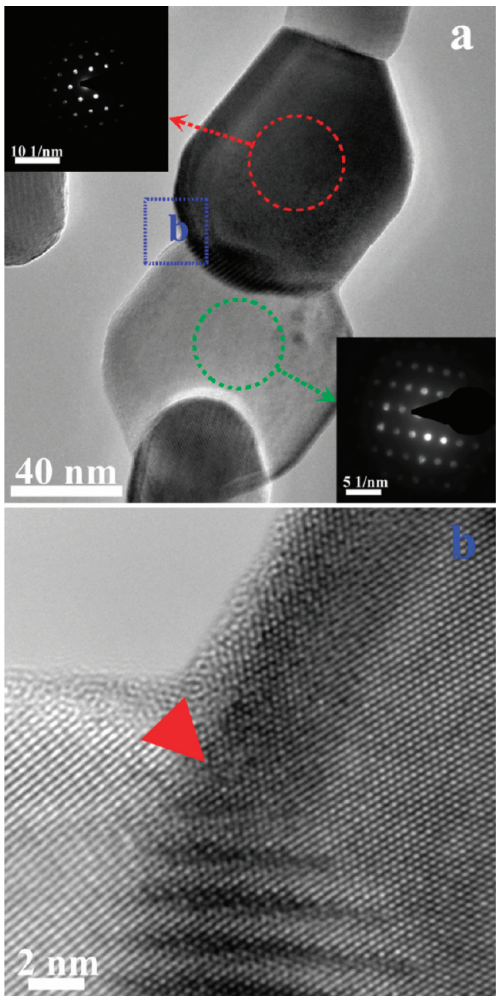

Figure 3. Structural analysis of the$BaFe_{12}O_{19}$ single-particle-chain nanofibers: (a) TEM image. Top-left inset shows a CBED pattern of the area 1 marked by a red circle. Bottom-right for area 2 marked by a green circle; (b) lattice-resolution HRTEM image of the interface of two neighbor crystallites on a single $BaFe_{12}O_{19}$ nanofiber marked by blue square in (a).

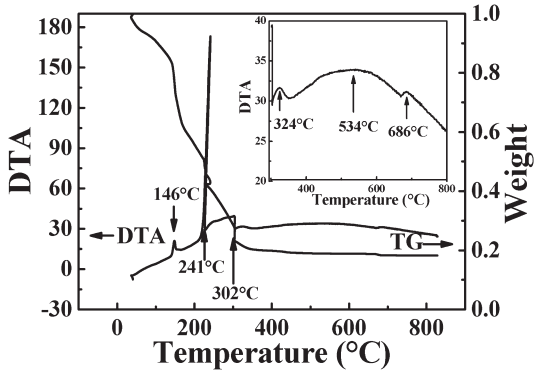

Figure 4. TG/DTA curves illustrating the transformation of the precursor nanofiber to $BaFe_{12}O_{19}$ single-particle-chain nanofibers.

electrospun PVP/barium nitrate/iron nitrate nonahydrate polymer composite nanofibers to $BaFe_{12}O_{19}$ single-particle-chain nanofibers. Limited to the length

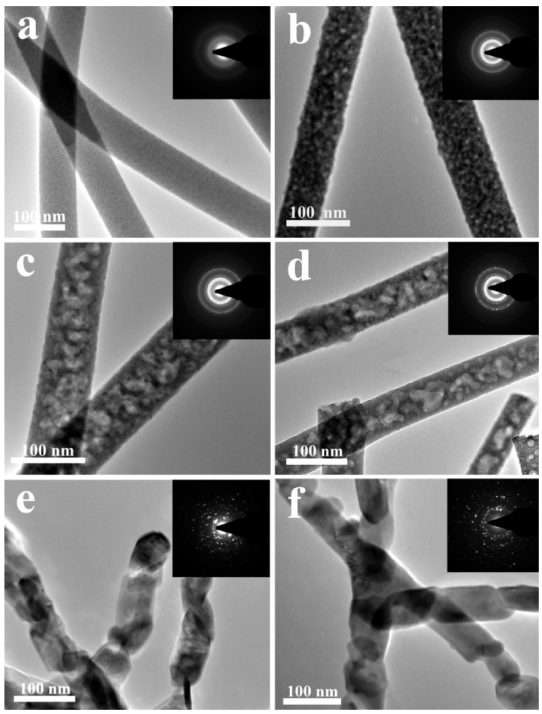

Figure 5. TEM images showing the morphology evolution during the process of calcination at six different temperatures and the inset showing the corresponding SAED: (a) 250 °C; (b) 400 °C; (c) 500 °C; (d) 600 °C; (e) 650 °C; (f) 800 °C.

of this paper, the detailed description and explanations of Figure 4 are presented in the Supporting Information. Combining the measurements of crystal structures of the nanofibers by XRD at seven temperature stages (see Figure S3 in the Supporting Information for details), it is suggested that the following reactions occur during the calcination process:

$$2Fe(NO_3)_3 \rightarrow Fe_2O_3 + NO_x$$

$$Ba(NO_3)_2 \rightarrow BaO + NO_x$$

$$BaO + CO_2 \rightarrow BaCO_3$$

$$BaCO_3 + Fe_2O_3 \rightarrow BaFe_2O_4 + CO_2$$

$$BaFe_2O_4 + 5Fe_2O_3 \rightarrow BaFe_{12}O_{19}$$

This observation is consistent with the reported $BaFe_{12}O_{19}$ nanoparticles.[28,29]

To further understand the formation mechanism of the $BaFe_{12}O_{19}$ single-particle-chain nanofibers, the morphologies and crystals of the electrospun PVP/barium nitrate/iron nitrate nonahydrate polymer composite nanofibers calcined at six different temperatures (250, 400, 500, 600, 650, and 800 °C) were observed (Figure 5) by TEM and SAED. This provides a direct insight of the formation of individual $BaFe_{12}O_{19}$ single-particle-chain nanofibers during the calcination. Figure 5a shows the nanofibers calcined at 250 °C, revealing that their surface morphology does not appear to change

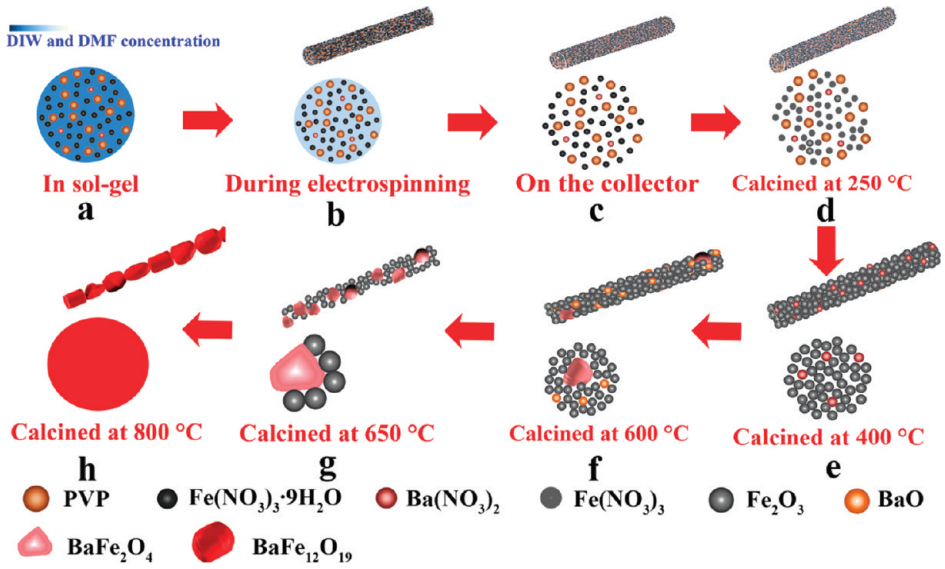

Figure 6. Schematic diagram of the formation mechanism of the $BaFe_{12}O_{19}$ single-particle-chain nanofibers. DIW and DMF concentrations decrease from blue to white.

from their amorphous nature. The corresponding SAED pattern shows fuzzy rings, suggesting an amorphous structure. When the temperature increased to 400 °C, particle-like structures on each nanofiber were formed (Figure 5b). This is probably due to the crystallization of Fe_2O_3 which came from the decomposition of iron nitrate confirmed by TG-DTA (Figure 4) and XRD (Figure S3). After 500 °C annealing, the grain sizes (Figure 5c) are larger than the size shown in Figure 5b, which is attributed to a coalescence of the small crystal grains of Fe_2O_3. The nanofiber surfaces also became much rougher. After calcination at 600 °C (Figure 5d), it is clearly seen that most of the nanoparticles have an approximate 20 nm size, much larger than the size in Figure 5c, and the average diameter of the nanofibers reduced to 80 nm. Combined with the TG-DTA (Figure 4) and XRD results (Figure S3), it is believed that a continuous nucleation of Fe_2O_3 nanocrystallites, formation of barium oxide and $BaFe_{12}O_{19}$ appears to accompany the $BaFe_2O_4$ generation at this temperature. Further annealing of the nanofibers at 650 °C for 2 h caused primary $BaFe_{12}O_{19}$ formation (Figure 5e). Both SAED patterns (the inset of Figure 5e) and XRD shown in Figure S3 proves that the hcp crystal structure of $BaFe_{12}O_{19}$ nanofibers has been formed. However, the nanofiber is not pure $BaFe_{12}O_{19}$, and the morphology is not a single-particle-chain-like structure. The final calcination at 800 °C for 2 h clearly caused the removal of all intermediate products and a further nucleation of individual $BaFe_{12}O_{19}$ nanoparticles on each nanofiber, which formed a single-particle-chain-like structure (Figure 5f). Their crystal structures detected by SAED (the inset of Figure 5f) and XRD (Figure S3) confirmed that pure $BaFe_{12}O_{19}$ nanofibers were obtained.

On the basis of these experiments and observations, a formation mechanism of the $BaFe_{12}O_{19}$ single-particle-chain nanofibers in this work is proposed, outlined in the schematic diagrams illustrated in Figure 6. It started from a sol–gel solution composed of PVP, DMF, DIW, barium nitrate, and iron nitrate nonahydrate prepared for electrospinning (Figure 6a). The solvents of DIW and DMF are believed to speed up the evaporation process before (Figure 6b) and after (Figure 6c) the PVP/barium nitrate/iron nitrate nonahydrate polymer composite nanofibers are electrospun and placed on a collector. At the preheating stage, the iron nitrite nonahydrate ($Fe(NO_3)_3 \cdot 6H_2O$) loses its water of hydration and the PVP starts to decompose (Figure 6d). When the specimen is calcined at a moderate temperature, the PVP is exhausted, and the $Fe(NO_3)_3$ decomposes into Fe_2O_3 and forms nucleations of ultrafine sizes (Figure 6e). When the heating temperature subsequently increases, the large Fe_2O_3 nucleations engulf their surrounded smaller crystallites (Figure 6f). Various sizes of crystallites are formed on a single nanofiber, as evidenced in Figure 5c. Simultaneously, the $Ba(NO_3)_2$ decomposes into BaO and reacts with the CO_2 and Fe_2O_3, which forms $BaFe_2O_4$ nanoparticles. The $BaFe_2O_4$ crystallites also begin to form, and the Fe_2O_3 grains increase their size (Figure 6g). During these processes between preheating and moderate temperatures (Figure 6d–g), the randomly unburned PVP pieces deriving from an uneven deposition velocity of PVP from the outside to inside of individual nanofibers form local spatial confinements with various sizes for the growth of crystallites. The various energy barriers of these confinements then lead to the formation of random orientations of the crystallites. At the same time, the nanofiber morphologies change from smooth to rough. As the temperature increases to a high calcination temperature for 2 h, the $BaFe_2O_4$ and Fe_2O_3 crystallites transform into

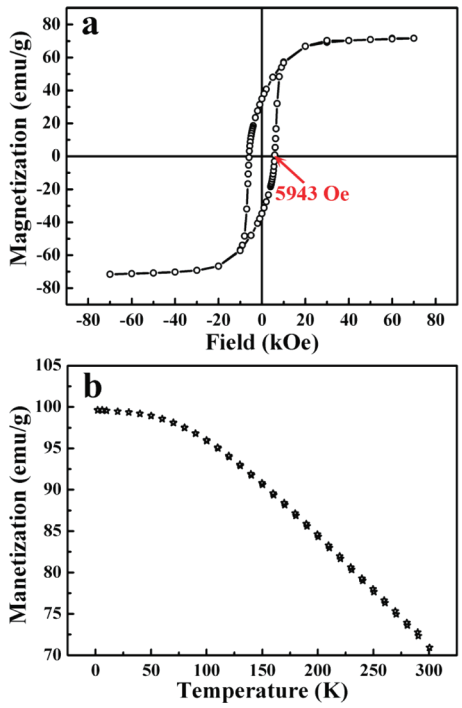

Figure 7. (a) Hysteresis loop of the $BaFe_{12}O_{19}$ single-particle-chain nanofibers measured at room temperature; (b) field-cooled (FC) curves of the $BaFe_{12}O_{19}$ single-particle-chain nanofibers measured at temperature ranging from 5 to 300 K with an applied magnetic field of 6 T.

$BaFe_{12}O_{19}$ crystallite. Simultaneously, the large crystals keep devouring their surrounded small crystals until eventually $BaFe_{12}O_{19}$ single-particle-chain fibers (Figure 6h) are formed and the metallic salt and polymer have been fully exhausted.

Magnetic Properties of the $BaFe_{12}O_{19}$ Single-Particle-Chain Nanofibers. SQUID technique was employed to investigate the dynamical magnetic properties of the $BaFe_{12}O_{19}$ single-particle-chain nanofibers. Figure 7a shows a typical hysteresis curve of the $BaFe_{12}O_{19}$ nanofibers measured at room temperature, indicating a coercivity of 5943 Oe. This value is larger than that of the $BaFe_{12}O_{19}$ nanowires prepared by AAO templates (2371 or 5760 Oe),[30] hollow fibers (2952 Oe),[31] thin films (3350 Oe using sol−gel processes, or 5100 using laser deposition),[17,32] nanoscale powders (5500 Oe),[33] and nanoparticles (approximately 3000 Oe).[34] Shape anisotropy derived from very large length-to-diameter ratios and high magnetocrystalline anisotropy are believed to be the main reasons for large coercivity force in the $BaFe_{12}O_{19}$ single-particle-chain nanofibers. This curve also shows that the saturated magnetization (M_s) of the $BaFe_{12}O_{19}$ single-particle-chain nanofibers at room temperature is 71.5 emu/g. This value is larger than that of the $BaFe_{12}O_{19}$ nanowires prepared by AAO templates (58.26 or 56.14 emu/g),[30] hollow fibers (51.56 emu/g),[31] nanoscale powders (59.36 emu/g),[33] and nanoparticles (51.9 and 56.5 emu/g).[34] Figure 7b shows a field-cooled curve of the $BaFe_{12}O_{19}$ single-particle-chain nanofibers

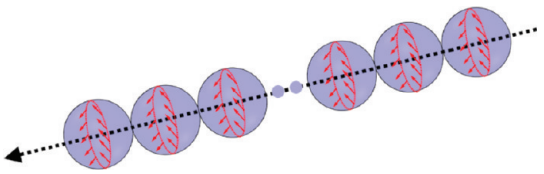

Figure 8. Schematic illustration of the magnetization reversal mechanism.

measured at temperature ranging from 5 to 300 K and with an applied magnetic field of 6 T. It is seen that M_s of the $BaFe_{12}O_{19}$ single-particle-chain nanofibers reaches 99.4 emu/g at 5 K, and that the M_s decreases with the increase of temperature.

To understand the magnetic behavior of the $BaFe_{12}O_{19}$ single-particles-chain nanofibers, the reported theoretical analysis of micromagnetism[26] is adapted. In this review, a coherent radius (R_{coh} = 3.655 l_{ex} for 1D magnetic materials) can be treated as a criteria whether the magnetization reversal mechanism of micro- or nanoscale system occurs through coherent rotation or curling. Under the case of $R < R_{coh}$, the magnetization process is governed by coherent rotation, but for the curling case $R > R_{coh}$; l_{ex} is the exchange length of the sample and is expressed in eq 1:

$$l_{ex} = \sqrt{\frac{A}{\mu_0 M_s^2}} \qquad (1)$$

where A is the exchange constant, -6.1×10^{-12} J·m^{-1} for $BaFe_{12}O_{19}$ and M_s is the saturated magnetization. The exchange length of $BaFe_{12}O_{19}$ is calculated to be approximately 5.9 nm. A 21.5 nm coherence radius for $BaFe_{12}O_{19}$ fibers is then calculated. In our case, the radius of the $BaFe_{12}O_{19}$ single-particle-chain nanofibers is 35 nm, determined by TEM observation, which is larger than the coherence radius. According to the criterion of coherent radii, our $BaFe_{12}O_{19}$ single-particle-chain nanofibers should have a curling mechanism for magnetization reversal (as illustrated in Figure 8).

For the curling process, the coercivity of the nanowire structure can be theoretically obtained from eq 2:[26,35]

$$H_c = \frac{2K_1}{\mu_0 M_s} - NM_s + \frac{cA}{\mu_0 M_s R^2} \qquad (2)$$

where K_1 is the magnetic anisotropic constant, 330×10^3 J·m^{-3} for $BaFe_{12}O_{19}$; N is the demagnetizing factor; c is a constant related to sample geometry, 6.6678 for a wire. However, this equation derives from a hypothesis that all easy axes of spheres on the wire aligned along the wire length axis, which is clearly not consistent with our case. As suggested by TEM observations, the individual particles of the $BaFe_{12}O_{19}$ single-particle-chain nanofibers have a random orientation and each particle is a single domain. That is, the easy axis of the individual particles on the $BaFe_{12}O_{19}$ single-particle-chain nanofiber is randomly oriented, rather than along the

nanofiber length axis as suggested using the hypothesis of eq 2. Therefore, eq 2 requires a modification for a better fit with our case. The first term of eq 2 represents a contribution of the magnetocrystalline anisotropy. When the angle between the easy axe(s) (or *c*-axis) of uniaxial single domain particle(s) and the applied field is only for π, the constant is 2.[36] When their angles are randomly distributed, the constant becomes 1, which is more appropriately fit with our case. The second term is attributed to the shape anisotropy. Due to the nanofibers' random orientation, the shape anisotropy of the nanofibers is equivalent to the nanoparticles that make up the nanofibers.[36] In our case, each particle on the nanofiber could be treated as a sphere for simplification, although it is not ideal in geometry. The third term represents a contribution of exchange energy which then stays the same. Therefore, eq 2 can be modified into (see Supporting Information for details):

$$H_c = \frac{K_1}{\mu_0 M_s} - \frac{1}{3}M_s + \frac{cA}{\mu_0 M_s R^2} \quad (3)$$

Using the geometry and saturation magnetization of the measured nanofiber, a calculation for the coercivity yields a value of 7131 Oe. This value is larger than the experimental findings of 5943 Oe, revealing a large discrepancy. Several reasons for this difference include a neglect of magnetostatic and exchange interaction between the neighborhood $BaFe_{12}O_{19}$ nanoparticles, too much simplification of particle's geometry, and the surface effect of individual particles. Nevertheless, the theoretical analysis still gives a preliminary insight of the magnetic origins of the $BaFe_{12}O_{19}$ single-particle-chain nanofibers.

CONCLUSIONS

In conclusion, we have demonstrated a fabrication method for $BaFe_{12}O_{19}$ single-particle-chain nanofibers using an electrospinning technique. Individual $BaFe_{12}O_{19}$ single-particle-chain nanofibers are found to have a continuous structure and uniform diameter, of which nanoparticles stacks side by side along the nanofiber axis. The hexagonal structure of bulk $BaFe_{12}O_{19}$ is proved to be preserves in the $BaFe_{12}O_{19}$ single-particle-chain nanofibers, and individual single crystallites on each $BaFe_{12}O_{19}$ single-particle-chain nanofibers have a random orientation. The experimental results reveal that the formation of $BaFe_{12}O_{19}$ single-particle-chain nanofibers mainly involves chemical reactions and phase transformations, and a formation mechanism is then proposed. The saturated magnetization of the $BaFe_{12}O_{19}$ single-particle-chain nanofibers is measured to be 71.5 emu/g at room temperature. The magnetization reversal mechanism of the $BaFe_{12}O_{19}$ single-particle-chain nanofibers is theoretically analyzed to fit a curling model. This work opens a new route for preparing large-scale production of various magnetic ferrite nanofibers with a high quality and length-to-diameter ratio. The new structural form of the single-particle-chain nanofibers is expected to have applications in the fields of biomagnetics, high-density data storage media, magnetic separation, microwave absorbers, switches, magnetic nanosensors, *etc*.

EXPERIMENTS AND METHODS

$BaFe_{12}O_{19}$ single-particle-chain nanofibers were prepared using the electrospinning techniques as follows. In a typical synthesis, 0.1 mmol barium nitrite ($Ba(NO_3)_2$, A.R., Alfa-Aesar Inc., USA), 1.2 mmol iron nitrite nonahydrate ($Fe(NO_3)_3 \cdot 9H_2O$, A.R., Alfa-Aesar Inc., USA), and 0.18 g of poly(vinyl pyrrolidone) (PVP, $M_w \approx 1\,300\,000$, Sigma-Aldrich Inc., USA) were dissolved into a mixed solution of 1.25 mL of deionized water (DIW) and 1.25 mL of *N*,*N*-dimethylformamide (DMF, A.R., Tianjin Chemical Corp., China) in a 5 mL vessel. The solution was continuously and vigorously agitated by a magnetic stirrer for 4 h. A homogeneous PVP/barium nitrate/iron nitrate precursor sol–gel solution was formed and then transferred into a syringe for electrospinning. The electrospinning process was performed by a dedicated electrospinning facility at 18.4 kV DC voltage, 15 cm spacing between needle tip and collector, and a feed rate was fixed with 0.4 mL/h. In comparison with traditional electrospinning methods, a special heating body was mounted in the end of syringe (see Figure S1 in the Supporting Information for details) to help the solubility of the $Ba(NO_3)_2$. The electrospun polymer composite fibers were collected using alumina crucibles and then calcined at 300 °C for 2 h, and then the temperature was increased to 800 °C for 2 h with a heating rate of 1 °C/min in air. The sample was finally allowed to cool to room temperature with the same heating rate of 1 °C/min in order to obtain a high level of crystalline structure.

The morphology, crystal structure, and chemical characterization of individual $BaFe_{12}O_{19}$ single-particle-chain nanofibers were analyzed at the nanoscale using a field-emission scanning electron microscope (FESEM, Hitachi S-4800, Japan), high-resolution transmission electron microscopy (HRTEM, Tecnai G^2 F30, FEI, USA) equipped with energy-dispersive X-ray analysis (EDX, Oxford Instrument, UK), high-angle annular dark and scanning transmission electron microscope (HAADF-STEM), and an X-ray diffraction instrument (XRD, Philips X'pert Pro MPD, The Netherlands). The transformation of the precursor nanofiber to $BaFe_{12}O_{19}$ single-particle-chain nanofibers was verified by a commercial thermogravimetry/differential thermal analysis (TG-DTA, Diamond, USA) with a heating rate 1 °C/min, XRD, and TEM techniques. Magnetic properties of the $BaFe_{12}O_{19}$ nanofibers were measured by superconducting quantum interference device (SQUID, MPMS-XL, Quantum Design, UK).

Conflict of Interest: The authors declare no competing financial interest.

Acknowledgment. This work was supported by the National Basic Research Program of China (973 program) (Grant No. 2012CB933104), the Natural Science Foundation of Gansu Province of China (Grant No. 1107RJZA221), the Fundamental Research Funds for Central Universities from the Ministry of Education of the People's Republic of China (Grant No. 860521), and the National Natural Science Foundation of China (Grant No. 11034004).

Supporting Information Available: Additional method information, schemes, HRTEM, XRD, TG/DTA, and the detailed description and explanations of formation of $BaFe_{12}O_{19}$. This material is available free of charge *via* the Internet at http://pubs.acs.org.

REFERENCES AND NOTES

1. Suh, J. S.; Lee, J. H.; Huh, Y. M.; Jun, Y.; Seo, J.; Jang, J.; Song, H. T.; Kim, S.; Cho, E. J.; Yoon, H. G.; *et al.* Artificially Engineered Magnetic Nanoparticles for Ultra-sensitive Molecular Imaging. *Nat. Med.* **2007**, *13*, 95–99.
2. Cheon, J.; Lee, J. H.; Jang, J. T.; Choi, J. S.; Moon, S. H.; Noh, S. H.; Kim, J. W.; Kim, J. G.; Kim, I. S.; Park, K. I. Exchange-Coupled Magnetic Nanoparticles for Efficient Heat Induction. *Nat. Nanotechnol.* **2011**, *6*, 418–422.
3. Zhang, Z. J.; Song, O. Shape Control and Associated Magnetic Properties of Spinel Cobalt Ferrite Nanocrystals. *J. Am. Chem. Soc.* **2004**, *126*, 6164–6168.
4. Hu, G.; Suzuki, Y. Negative Spin Polarization of Fe_3O_4 in Magnetite/Manganite-Based Junctions. *Phys. Rev. Lett.* **2002**, *89*, 276601.
5. Ederer, C.; Spaldin, N. A. Weak Ferromagnetism and Magnetoelectric Coupling in Bismuth Ferrite. *Phys. Rev. B* **2005**, *71*, 060401.
6. Parkin, S. S. P.; Hayashi, M.; Thomas, L. Magnetic Domain-Wall Racetrack Memory. *Science* **2008**, *320*, 190–194.
7. Gregg, J. F.; Petej, I.; Jouguelet, E.; Dennis, C. Spin Electronics—A Review. *J. Phys. D: Appl. Phys.* **2002**, *35*, R121–R155.
8. Lee, S. B.; Son, S. J.; Reichel, J.; He, B.; Schuchman, M. Magnetic Nanotubes for Magnetic-Field-Assisted Bioseparation, Biointeraction, and Drug Delivery. *J. Am. Chem. Soc.* **2005**, *127*, 7316–7317.
9. Miyawaki, J.; Yudasaka, M.; Imai, H.; Yorimitsu, H.; Isobe, H.; Nakamura, E.; Iijima, S. *In Vivo* Magnetic Resonance Imaging of Single-Walled Carbon Nanohorns by Labeling with Magnetite Nanoparticles. *Adv. Mater.* **2006**, *18*, 1010–1014.
10. Arruebo, M.; Fernández-Pacheco, R.; Ibarra, M. R.; Santamaría, J. Magnetic Nanoparticles for Drug Delivery. *Nano Today* **2007**, *2*, 22–32.
11. Kojima, H. Fundamental Properties of Hexagonal Ferrites with Magnetoplumbite Structure. *Handbook of Ferromagnetic Materials*; Elsevier: Amsterdam, 1982; Vol. 3, pp 305–391.
12. Tsung-Shune, C. Permanent Magnet Films for Applications in Microelectromechanical Systems. *J. Magn. Magn. Mater.* **2000**, *209*, 75–79.
13. Nakamura, H.; Ohmi, F.; Kaneko, Y.; Sawada, Y.; Watada, A.; Machida, H. Cobalt-Titanium Substituted Barium Ferrite Films for Magneto-Optical Memory. *J. Appl. Phys.* **1987**, *61*, 3346–3348.
14. Uher, J.; Hoefer, W. J. R. Tunable Microwave and Millimeter-Wave Band-Pass Filters. *IEEE Trans. Microwave Theory Tech.* **1991**, *39*, 643–653.
15. Jalli, J.; Hong, Y. K.; Bae, S.; Lee, J. J.; Abo, G. S.; Lyle, A.; Gee, S. H.; Lee, H.; Mewes, T.; Sur, J. C.; *et al.* Growth and Characterization of 144 μm Thick Barium Ferrite Single Crystalline Film for Microwave Device Application. *J. Appl. Phys.* **2009**, *105*, 07A511.
16. Tsukahara, Y.; Yamauchi, T.; Sakata, T.; Mori, H.; Chikata, T.; Katoh, S.; Wada, Y. Barium Ferrite Powders Prepared by Microwave-Induced Hydrothermal Reaction and Magnetic Property. *J. Magn. Magn. Mater.* **2009**, *321*, 8–11.
17. Lu, Y. F.; Song, W. D. Properties of $BaFe_{12}O_{19}$ Films Prepared by Laser Deposition with *In Situ* Heating and Post Annealing. *Appl. Phys. Lett.* **2000**, *76*, 490–492.
18. Han, X. J.; Xu, P.; Jiang, J. J.; Wang, X. H.; Li, X. D.; Wen, A. H. Synthesis and Characterization of Novel Coralloid Polyaniline/$BaFe_{12}O_{19}$ Nanocomposites. *J. Phys. Chem. C* **2007**, *111*, 12603–12608.
19. Fu, L.; Liu, X.; Zhang, Y.; Dravid, V. P.; Mirkin, C. A. Nanopatterning of "Hard" Magnetic Nanostructures *via* Dip-Pen Nanolithography and a Sol-Based Ink. *Nano Lett.* **2003**, *3*, 757–760.
20. Formhals, A. Process and Apparatus for Preparing Artificial Threads. U.S. Patent 1975504, 1934.
21. Vacanti, J. P.; Yoshimoto, H.; Shin, Y. M.; Terai, H. A Biodegradable Nanofiber Scaffold by Electrospinning and Its Potential for Bone Tissue Engineering. *Biomaterials* **2003**, *24*, 2077–2082.
22. Xia, Y. N.; Li, D. Direct Fabrication of Composite and Ceramic Hollow Nanofibers by Electrospinning. *Nano Lett.* **2004**, *4*, 933–938.
23. Li, D.; Xia, Y. Electrospinning of Nanofibers: Reinventing the Wheel? *Adv. Mater.* **2004**, *16*, 1151–1170.
24. Pinto, N. J.; Johnson, A. T.; MacDiarmid, A. G.; Mueller, C. H.; Theofylaktos, N.; Robinson, D. C.; Miranda, F. A. Electrospun Polyaniline/Polyethylene Oxide Nanofiber Field-Effect Transistor. *Appl. Phys. Lett.* **2003**, *83*, 4244–4246.
25. Reneker, D. H.; Chun, I. Nanometre Diameter Fibres of Polymer, Produced by Electrospinning. *Nanotechnology* **1996**, *7*, 216–223.
26. Skomski, R. Nanomagnetics. *J. Phys.: Condens. Matter* **2003**, *15*, R841–R896.
27. Halder, A.; Ravishankar, N. Ultrafine Single-Crystalline Gold Nanowire Arrays by Oriented Attachment. *Adv. Mater.* **2007**, *19*, 1854–1858.
28. Steier, H. P.; Requena, J.; Moya, J. S. Transmission Electron Microscopy Study of Barium Hexaferrite Formation from Barium Carbonate and Hematite. *J. Mater. Res.* **1999**, *14*, 3647–3652.
29. Zhong, W.; Ding, W.; Zhang, N.; Hong, J.; Yan, Q.; Du, Y. Key Step in Synthesis of Ultrafine $BaFe_{12}O_{19}$ by Sol–Gel Technique. *J. Magn. Magn. Mater.* **1997**, *168*, 196–202.
30. Huang, Y.; Li, Y. Q.; Yan, L.; Qi, S. H.; Miao, L.; Wang, Y.; Wang, Q. F. Synthesis and Magnetic Properties of Ordered Barium Ferrite Nanowire Arrays in AAO Template. *Appl. Surf. Sci.* **2011**, *257*, 8974–8980.
31. Guan, J. G.; Mou, F. Z.; Sun, Z. G.; Fan, X. A.; Tong, G. X. *In Situ* Generated Dense Shell-Engaged Ostwald Ripening: A Facile Controlled-Preparation for $BaFe_{12}O_{19}$ Hierarchical Hollow Fiber Arrays. *J. Solid State Chem.* **2010**, *183*, 736–743.
32. Qiu, J.; Gu, M. Magnetic Nanocomposite Thin Films of $BaFe_{12}O_{19}$ and TiO_2 Prepared by Sol–Gel Method. *Appl. Surf. Sci.* **2005**, *252*, 888–892.
33. Huang, J. G.; Zhuang, H. R.; Li, W. L. Synthesis and Characterization of Nano Crystalline $BaFe_{12}O_{19}$ Powders by Low Temperature Combustion. *Mater. Res. Bull.* **2003**, *38*, 149–159.
34. Yu, H. F.; Lin, H. Y. Preparation and Thermal Behavior of Aerosol-Derived $BaFe_{12}O_{19}$ Nanoparticles. *J. Magn. Magn. Mater.* **2004**, *283*, 190–198.
35. Aharoni, A. The Nucleation Problem. *Introduction to the Theory of Ferromagnetism*, 2nd ed.; Oxford University Press: Oxford, 2001; pp 186–193.
36. Zhong, W. D. The Magnetization Reversal Mechanism of Magnetic Materials. *Ferromagnetism*; Scientific Press of China: 1998; Vol. 2, p 338.